International Journal of Solids and Structures 48 (2011) 2255–2263

Contents lists available at ScienceDirect

International Journal of Solids and Structures

journal homepage: www.elsevier.com/locate/ijsolstr

Analysis of stress concentration around a spheroidal cavity under asymmetric dynamic loading

R. Paskaramoorthy *, S. Bugarin, R.G. Reid

DST/NRF Centre of Excellence in Strong Materials and RP/Composites Facility, School of Mechanical, Industrial and Aeronautical Engineering, University of the Witwatersrand, Johannesburg Private Bag 3, Wits 2050, South Africa

ARTICLE INFO

Article history:
Received 15 October 2010
Received in revised form 25 January 2011
Available online 9 April 2011

Keywords:
Stress concentration
Dynamic loading
Porous material

ABSTRACT

The fracture and fatigue properties of porous materials are strongly influenced by stress concentrations around the pores. In addition, failure of structural components initiates at locations of high stress concentration which is often caused by holes, inclusions or other discontinuities. In view of this, the stress concentration around a spheroidal cavity embedded in an elastic medium is studied under dynamic loading conditions. While solutions abound for static loads, only limited solutions exist for dynamic loads. The stress field around a spheroidal cavity is determined by using a hybrid methodology that combines the finite element technique with a spherical wave function expansion method. The stress concentrations within the matrix are found to be dependent on the frequency of excitation, aspect ratio of the cavity and the Poisson's ratio of the matrix. The study reveals that dynamic stress concentrations can reach much higher values than those encountered under static loading.

1. Introduction

A certain volume of empty space tends to occur in any material. This space is distributed within the solid material in the form of cavities of various shapes and sizes. When the material is subjected to a load, a stress concentration develops around the cavities. Determination of this stress concentration is a problem of considerable interest in many branches of material science and applied mechanics, since it effectively lowers the overall strength, fracture and fatigue properties of the material.

The influence of stress concentrations on the mechanical properties of porous materials has long been recognised (Hasselman and Fulrath, 1964; Wang, 1984; Panakkal et al., 1990; Danninger et al., 1993; Maitra and Phani, 1994; Boccaccini et al., 1995; Boccaccini, 1998). For instance, an equation of the form

$$E = E_0(1-p)^m$$

has been shown to predict the Young's modulus (E) of sintered powder metals and porous ceramics (Maitra and Phani, 1994). In the above, E_0 is the Young's modulus of the nonporous material, p is the volume fraction of pores and m is related to the stress concentration factor around the pores. Similar relationships have also been proposed to calculate the fracture strength of porous materials (Danninger et al., 1993).

In the applied mechanics literature, the study of stress concentrations goes back to Kirsch (1898) who considered an infinite plate subjected to static tensile loading. Many investigations have since been conducted for cavities and other forms of stress raisers such as notches, inclusions and reinforcements. The review articles by Sternberg (1958) and Neuber and Hahn (1966), although somewhat dated, provide a wealth of information on the subject which continues to attract the attention of researchers. The monograph by Tan (1994) provides a comprehensive coverage on stress concentrations in laminated composites. Some recent works on stress concentrations caused by holes or cavities may be found, for instance, in the works of Yu et al. (2008), Yang et al. (2008), and Prokic et al. (2009).

All these investigations considered static loading, where the inertia of the medium can be ignored. This simplification cannot be made when dynamic loading is considered. The energy of the dynamic load is transmitted in the form of waves travelling through the medium. At a discontinuity, these waves are reflected, refracted and scattered giving rise to elevated local stress states. The phenomenon of dynamic stress concentration may, therefore, be regarded as one of scattering of elastic waves.

Scattering of elastic waves by a discontinuity such as a cavity or an inclusion has been the subject of many investigations. The excellent monograph by Pao and Mow (1973) gives a comprehensive coverage of this and other related subjects. Solutions for two dimensional problems have been presented by Bogan and Hinders (1993) and others. In three dimensions, scattering by spherical, spheroidal and ellipsoidal discontinuities has been studied by Datta (1977), Willis (1980), Paskaramoorthy et al. (1988) and many others. More recent contributions on this subject have been presented by Meguid and Wang (1997), Hayir and Bakirtas (2004),

* Corresponding author. Tel.: +27 117177310; fax: +27 117177049.
E-mail address: ratnam.paskaramoorthy@wits.ac.za (R. Paskaramoorthy).

0020-7683/$ - see front matter © 2011 Elsevier Ltd. All rights reserved.
doi:10.1016/j.ijsolstr.2011.04.001

Iturrarán-Viveros et al. (2008), and Yu and Dravinski (2009). Unlike the above studies where the emphasis was on the scattered wave pattern, results for dynamic stress concentration are somewhat limited. One of the early works on this subject was by Ying and Truell (1956) who studied the dynamic stress field around a rigid spherical inclusion. In recent years, Paskaramoorthy and his co-workers (1999, 2000, 2009) have presented dynamic stress concentration results for spherical and spheroidal geometries embedded in an elastic medium. Solutions for poroelastic and functionally graded materials have also been reported in the literature. In this regard, an interested reader is referred to the works of Wang et al. (2005), Fang et al. (2009) and the reference works cited therein.

In this paper, the work of Paskaramoorthy and Meguid (2000) is extended for a prolate spheroidal cavity subjected to an asymmetric dynamic load. Even though the geometry is axisymmetric, the loading is asymmetric rendering the problem three dimensional. As a result, all three displacement components need to be considered in the formulation rather than just the two in the axisymmetric problem studied previously (Paskaramoorthy and Meguid, 2000). In addition, in the previous study it was found that the dynamic stress concentrations could be 100% greater than the quasi-static values. However, due to the asymmetric nature of the loading considered in this paper, these effects are expected to be different.

The objective of this work is to study the stress state in the matrix medium and quantify the severity of the stress concentration on the surface of the cavity for a range of frequencies and cavity aspect ratios. For simplicity, the effect of the interaction of neighbouring cavities is ignored. The presence of nearby cavities causes multiple scattering. This subject is very complex and it will be dealt with in a future communication. Fig. 1a shows the geometry of a single prolate spheroidal cavity embedded in an infinitely large matrix; the z-axis is the axis of symmetry. The cavity is excited by an incident plane shear wave propagating along the z-axis and polarised along the x-axis. The problem could be solved by using a number of different methods such as spherical wave function expansion technique (Sanchez-Sesma, 1983; Lee, 1984; Eshraghi and Dravinski, 1989a,b), indirect boundary integral equation method (Mossessian and Dravinski, 1989c, 1990), and boundary element method (Manolis and Beskos, 1988). In addition, the method of finite elements could also be used in conjunction with infinite elements, absorbing surfaces or non-reflecting boundaries (Givoli, 1991; Sarma et al., 1998). All of these methods could possibly give a highly accurate solution for the stress concentration in the matrix medium. In the present paper, a different approach that combines the finite element methodology with the wave function expansion technique is used. To this end, a fictitious spherical boundary B is drawn such that it encloses the cavity and a finite region of the elastic medium. The region between the cavity and the boundary B is referred to as the *interior region* and is modelled by using an assembly of finite elements. The solution in the region exterior to the boundary B is represented by spherical wave functions. Equations to determine displacements for the nodes lying on the boundary B are obtained by imposing the continuity of the displacements and traction forces between the interior and exterior regions. These, in turn, are used to obtain both the displacements of the interior nodes and the unknown coefficients associated with the spherical wave functions. The displacements are then used to determine the stress field.

2. Statement of the problem

The surface of the cavity, denoted by S, is defined by

$$\frac{x^2}{a^2}+\frac{y^2}{a^2}+\frac{z^2}{b^2}=1. \tag{1}$$

where a and b are the semi-axes of the cavity along the x and z axes respectively. The domain of the medium is denoted by D. The material is assumed to be homogeneous, linearly elastic and isotropic. Only time-harmonic excitation is considered. Thus, all the field quantities have a time dependence $e^{-i\omega t}$, where ω is the frequency of excitation.

The equation of motion of the domain D for the steady state is specified by

$$(\lambda+2\mu)\nabla(\nabla\cdot\mathbf{U})-\mu\nabla\times\nabla\times\mathbf{U}+\rho\omega^2\mathbf{U}=0 \quad \mathbf{x}\in D, \tag{2}$$

where $\mathbf{U}=(u,v,w)$ is the displacement vector, $\mathbf{x}$ is the position vector, ρ is the density, and λ and μ are the Lamé constants of the medium.

The boundary conditions on the surface S of the cavity are of the form

$$\sigma_{ij}n_j=0 \quad \mathbf{x}\in S, \tag{3}$$

where n is the unit normal vector to the surface S and the summation convention for repeated indices is assumed. A solution to Eq. (2) that satisfies Eq. (3) is sought. In addition, the solution should be regular at infinity.

3. Formulation of the problem

3.1. Interior region

The interior region contains the cavity and a small portion of the surrounding matrix. This region is modelled by using 9-noded isoparametric finite elements. A typical finite element mesh is shown in Fig. 2 where the mid-side and interior nodes are omitted for clarity. The formulation is presented in the cylindrical coordinate system (r,ϕ,z) shown in Fig. 1b. In the analysis of axisymmetric bodies subjected to non-axisymmetric loadings, both loads and displacements are expanded in Fourier series in the circumferential direction. For instance, the displacement components may be written, in cylindrical coordinate system, as

$$u_r(r,\phi,z,t)=\sum_{m=0}^{\infty}[\bar{u}_{rm}(r,z)\cos m\phi+\hat{u}_{rm}(r,z)\sin m\phi]e^{-i\omega t}, \tag{4}$$

$$u_z(r,\phi,z,t)=\sum_{m=0}^{\infty}[\bar{u}_{zm}(r,z)\cos m\phi+\hat{u}_{zm}(r,z)\sin m\phi]e^{-i\omega t}, \tag{5}$$

$$u_\phi(r,\phi,z,t)=\sum_{m=0}^{\infty}\left[-\bar{u}_{\phi m}(r,z)\sin m\phi+\hat{u}_{\phi m}(r,z)\cos m\phi\right]e^{-i\omega t}, \tag{6}$$

where $i=\sqrt{-1}$, the overbar denotes amplitude of the displacement components symmetric about the $\phi=0$ axis, the hat denotes the antisymmetric components and m is the circumferential harmonic number. The negative sign before $\bar{u}_{\phi m}(r,z)$ has the effect of giving identical stiffness matrices for both symmetric and antisymmetric components. The primary unknowns in this formulation are amplitudes of the displacement components which are functions of r and z only and do not depend upon ϕ. Since the polarization of the incident wave is in the xz-plane, the resulting loading will be symmetric about $\phi=0$. Consequently, only the symmetric part of the displacement components is used. This paper considers only the case of incident wave propagating along the z-axis with polarization along the x-axis. This results in further simplification in that only one harmonic number, namely $m=1$, survives. Consequently, the displacement field can be written as

$$u_r(r,\phi,z,t)=\bar{u}_r(r,z)\cos\phi e^{-i\omega t}, \tag{7}$$

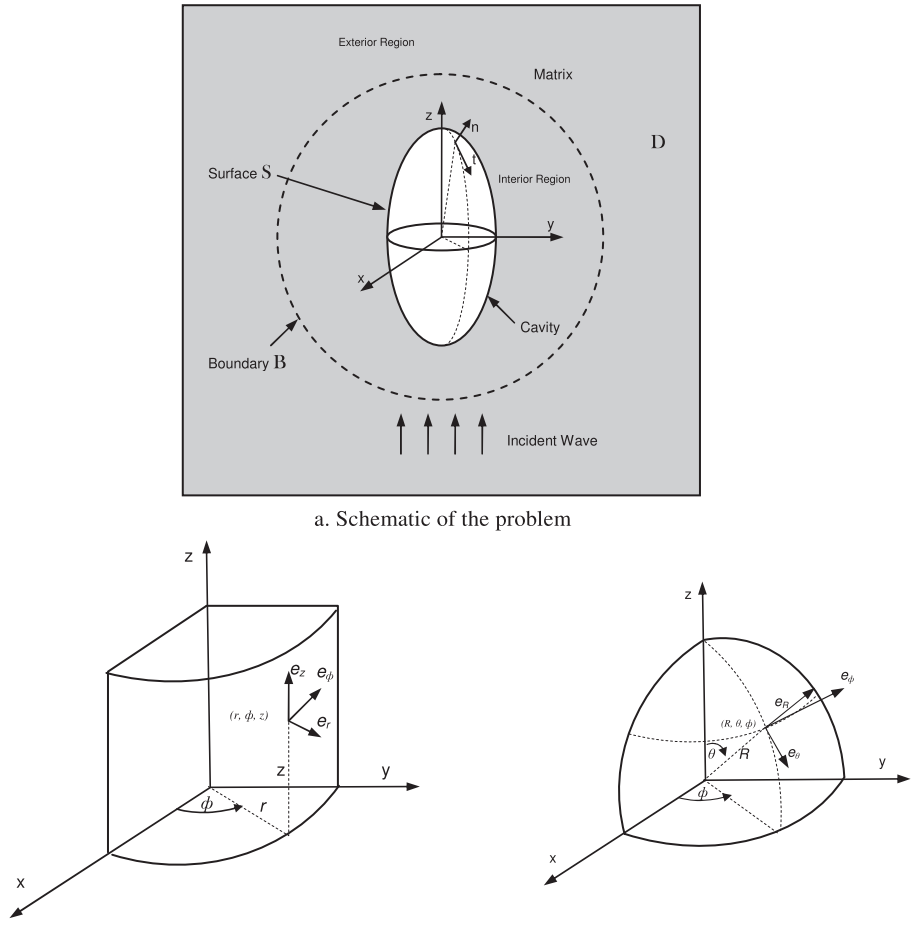

Fig. 1. Problem geometry with cylindrical and spherical coordinate systems.

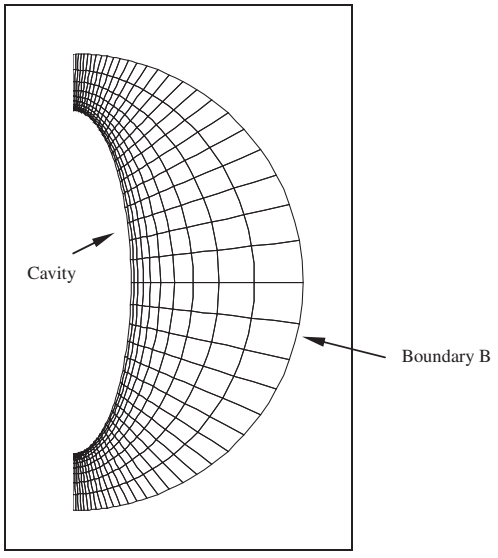

Fig. 2. Finite element mesh of the interior region for $b/a = 3$

$$u_z(r,\phi,z,t) = \bar{u}_z(r,z)\cos\phi e^{-i\omega t}, \tag{8}$$

$$u_\phi(r,\phi,z,t) = -\bar{u}_\phi(r,z)\sin\phi e^{-i\omega t}, \tag{9}$$

where the index m in the subscript of barred terms has been dropped for notational convenience.

The amplitude of displacements within an element is interpolated from the nodal displacement amplitude as

$$\{\bar{u}\} = [N]\{\bar{q}\}, \tag{10}$$

where $[N]$ contains interpolation functions, $\{\bar{q}\}$ is the vector of nodal displacement amplitudes, and

$$\{\bar{u}\} = \langle \bar{u}_r \quad \bar{u}_z \quad \bar{u}_\phi \rangle^T. \tag{11}$$

In the above, the superscript T denotes transpose. Explicit expressions for $[N]$ may be found in the book by Cook et al. (1989) or in many other standard reference books on finite elements.

The governing equation of motion, which can be obtained by following the conventional finite element methodology for axisymmetric elements subjected to nonaxisymmetric loads (Cook et al., 1989), is given by

$$[S]\{\bar{q}\} = \{\bar{P}\}, \tag{12}$$

where

$$[S] = [K] - \omega^2[M], \tag{13}$$

in which $[K]$ and $[M]$ are the respective stiffness and consistent mass matrices of the interior region, $\{\bar{q}\}$ is the vector of nodal displacement amplitudes, and $\{\bar{P}\}$ is the vector of nodal load amplitudes.

If the vector $\{\bar{q}\}$ is separated into two parts, $\{\bar{q}_B\}$ corresponding to the amplitude of nodal displacements at the boundary B, and

$\{\bar{q}_I\}$ corresponding to the amplitude of nodal displacements elsewhere in the interior region, Eq. (13) can be written as

$$\begin{bmatrix} S_{II} & S_{IB} \\ S_{BI} & S_{BB} \end{bmatrix} \begin{Bmatrix} \bar{q}_I \\ \bar{q}_B \end{Bmatrix} = \begin{Bmatrix} 0 \\ \bar{P}_B \end{Bmatrix}, \tag{14}$$

in which the $\{\bar{P}_B\}$ represent the amplitudes of interaction forces between the interior and exterior regions.

3.2. Exterior region

The incident and scattered waves are denoted by the superscripts i and s respectively. The displacement vector $\mathbf{U}$ has contributions from both incident and scattered waves. While the incident wave field is known, the scattered wave field is unknown.

3.2.1. Scattered waves

A solution for $\mathbf{U}^s$ satisfying Eq. (2) and far-field radiation conditions can be written in the spherical coordinate system of Fig. 1c as (Pao and Mow, 1973)

$$\mathbf{U} = \nabla\varphi + \frac{1}{\beta}\nabla \times \nabla(R\chi) \times \mathbf{e}_R + \nabla(R\psi) \times \mathbf{e}_R, \tag{15}$$

where $\mathbf{e}_R$ is the unit vector in the R–direction and φ, χ and ψ are given by

$$\varphi(R,\theta,\phi) = \sum a_{1n} h_n(\alpha R) P_n^1(\cos\theta)\cos\phi e^{-i\omega t}, \tag{16}$$

$$\chi(R,\theta,\phi) = \sum a_{2n} h_n(\beta R) P_n^1(\cos\theta)\cos\phi e^{-i\omega t}, \tag{17}$$

$$\psi(R,\theta,\phi) = \sum b_{3n} h_n(\beta R) P_n^1(\cos\theta)\sin\phi e^{-i\omega t}, \tag{18}$$

In the above, and in the following, all the summations are over integral values of n from one to infinity, a_{1n}, a_{2n} and b_{3n} are as yet unknown amplitude coefficients, h_n is the spherical Hankel function of the first kind and order n, P_n^1 is the associated Legendre function of first order and degree n, α and β are wave numbers defined by

$$\alpha^2 = \frac{\omega^2\rho}{(\lambda+2\mu)}; \quad \beta^2 = \frac{\omega^2\rho}{\mu}. \tag{19}$$

Substituting Eqs. (16)–(18) in Eq. (15), we obtain

$$u_R(R,\theta,\phi,t) = \bar{u}_R(R,\theta)\cos\phi e^{-i\omega t} = e^{-i\omega t}\cos\phi \sum \bar{u}_R^n, \tag{20}$$

$$u_\theta(R,\theta,\phi,t) = \bar{u}_\theta(R,\theta)\cos\phi e^{-i\omega t} = e^{-i\omega t}\cos\phi \sum \bar{u}_\theta^n, \tag{21}$$

$$u_\phi(R,\theta,\phi,t) = \bar{u}_\phi(R,\theta)\sin\phi e^{-i\omega t} = e^{-i\omega t}\sin\phi \sum \bar{u}_\phi^n, \tag{22}$$

where

$$\bar{u}_R^n = a_{1n}\left[\frac{n}{R}h_n(\alpha R) - \alpha h_{n+1}(\alpha R)\right]P_n^1 + a_{2n}n(n+1)\frac{h_n(\beta R)}{\beta R}P_n^1, \tag{23}$$

$$\bar{u}_\theta^n = a_{1n}\frac{h_n(\alpha R)}{R}\frac{dP_n^1}{d\theta} + a_{2n}\left[(n+1)\frac{h_n(\beta R)}{\beta R} - h_{n+1}(\beta R)\right]\frac{dP_n^1}{d\theta} + b_{3n}Z_n(\beta R)\frac{P_n^1}{\sin\theta}, \tag{24}$$

$$-\bar{u}_\phi^n = a_{1n}\frac{h_n(\alpha R)}{R}\frac{P_n^1}{\sin\theta} + a_{2n}\left[(n+1)\frac{h_n(\beta R)}{\beta R} - h_{n+1}(\beta R)\right]\frac{P_n^1}{\sin\theta} + b_{3n}h_n(\beta R)\frac{dP_n^1}{d\theta}. \tag{25}$$

In the above, the argument $(\cos\theta)$ for P_n^1 and its derivative has been suppressed for notational convenience. The stress field associated with the displacements of Eqs. (20)–(22) are given by

$$\sigma_{RR}(R,\theta,\phi,t) = \bar{\sigma}_{RR}(R,\theta)\cos\phi e^{-i\omega t} = e^{-i\omega t}\cos\phi\sum\bar{\sigma}_{RR}^n \tag{26}$$

$$\sigma_{R\theta}(R,\theta,\phi,t) = \bar{\sigma}_{R\theta}(R,\theta)\cos\phi e^{-i\omega t} = e^{-i\omega t}\cos\phi\sum\bar{\sigma}_{R\theta}^n \tag{27}$$

$$\sigma_{R\phi}(R,\theta,\phi,t) = \bar{\sigma}_{R\phi}(R,\theta)\sin\phi e^{-i\omega t} = e^{-i\omega t}\sin\phi\sum\bar{\sigma}_{R\phi}^n, \tag{28}$$

where

$$\bar{\sigma}_{RR}^n = a_{1n}\frac{2\mu}{R^2}\left[\left(n^2 - n - \frac{1}{2}\beta^2R^2\right)h_n(\alpha R) + 2\alpha R h_{n+1}(\alpha R)\right]P_n^1 + a_{2n}\frac{2\mu}{R^2}\frac{n(n+1)}{\beta}[(n-1)h_n(\beta R) - \beta R h_{n+1}(\beta R)]P_n^1, \tag{29}$$

$$\bar{\sigma}_{R\theta}^n = a_{1n}\frac{2\mu}{R^2}[(n-1)h_n(\alpha R) - \alpha R h_{n+1}(\alpha R)]\frac{dP_n^1}{d\theta} + a_{2n}\frac{2\mu}{R^2} \times \frac{1}{\beta}\left[\left(n^2 - 1 - \frac{1}{2}\beta^2R^2\right)h_n(\beta R) + \beta R h_{n+1}(\beta R)\right]\frac{dP_n^1}{d\theta} - b_{3n}\frac{\mu}{R}[\beta R h_{n+1}(\beta R) - (n-1)h_n(\beta R)]\frac{P_n^1}{\sin\theta}, \tag{30}$$

$$-\bar{\sigma}_{R\phi}^n = a_{1n}\frac{2\mu}{R^2}[(n-1)h_n(\alpha R) - \alpha R h_{n+1}(\alpha R)]\frac{P_n^1}{\sin\theta} + a_{2n}\frac{2\mu}{R^2} \times \frac{1}{\beta}\left[\left(n^2 - 1 - \frac{1}{2}\beta^2R^2\right)h_n(\beta R) + \beta R h_{n+1}(\beta R)\right]\frac{P_n^1}{\sin\theta} - b_{3n}\frac{\mu}{R}[\beta R h_{n+1}(\beta R) - (n-1)h_n(\beta R)]\frac{dP_n^1}{d\theta}, \tag{31}$$

Let p be the number of significant terms in Eqs. (20)–(22), and (26)–(28). Evaluating Eqs. (20)–(22) at each node lying on the boundary B, we can construct a matrix $[G]$ relating the nodal displacement amplitudes to the unknown coefficients as.

$$\{\bar{q}_B^s\}_{sph} = [G]\{a\}, \tag{32}$$

where $\{\bar{q}_B^s\}_{sph}$ is the array of amplitude of displacements, in spherical coordinates, at the nodes on the boundary B, $\{a\}$ contains the unknown coefficients a_{1n}, a_{2n} and b_{3n} with $n = 1,\ldots,p$. It can be seen that the matrix $[G]$ is complex valued. If N_B is the number of nodes on the boundary B, the $[G]$ matrix will have dimensions $3N_B \times 3p$.

Similarly, a relationship between the amplitude of nodal forces, $\{\bar{P}_B^s\}$, at the boundary B and the unknown coefficients, $\{a\}$, can be established by evaluating the stresses σ_{RR}^s, $\sigma_{R\theta}^s$ and $\sigma_{R\phi}^s$ at each node on B and multiplying them by the corresponding tributary area:

$$\{\bar{P}_B^s\}_{sph} = [F]\{a\}. \tag{33}$$

A relationship between the load vector $\{\bar{P}_B^s\}$ and the displacement vector $\{\bar{q}_B^s\}$ can now be established by eliminating $\{a\}$ from Eqs. (32) and (33). To this end, we first write the Eq. (32) as (see Appendix)

$$\{a\} = [H]\{\bar{q}_B^s\}_{sph}; \quad [H] = ([G^*]^T[G])^{-1}[G^*]^T \tag{34}$$

and substitute it in Eq. (33) to obtain

$$\{\bar{P}_B^s\}_{sph} = [F][H]\{\bar{q}_B^s\}_{sph}. \tag{35}$$

The arrays $\{\bar{P}_B^s\}$ and $\{\bar{q}_B^s\}$ in the above equation are in the spherical coordinate system. When they are transformed into cylindrical coordinates, Eq. (35) takes the form

$$\{\bar{P}_B^s\} = [S_f]\{\bar{q}_B^s\}, \tag{36}$$

where

$$[S_f] = [L]^t[F][H][L],$$

in which $[L]$ is the transformation matrix.

3.2.2. Incident wave

Let the incident wave be represented by the displacement field in the Cartesian coordinate system as

$$\mathbf{U} = \mathbf{e}_x e^{i\beta z - i\omega t}, \tag{37}$$

where $\mathbf{e}_x$ is the unit vector in the x direction. This being a plane wave propagating in the z direction, its extent covers the whole x–y plane. The components of the displacement field can be expressed in the cylindrical coordinate system of Fig. 1b as

$$u_r^i = e^{i\beta z}\cos\phi e^{-i\omega t}, \tag{38}$$

$$u_\phi^i = -e^{i\beta z}\sin\phi e^{-i\omega t}, \tag{39}$$

$$u_z^i = 0, \tag{40}$$

It can be seen that the variation of the displacement components with respect to the angular coordinate ϕ is similar those presented in Eqs. (7)–(9). The resulting stress field is given by

$$\sigma_{rz}^i = i\mu\beta e^{i\beta z}\cos\phi e^{-i\omega t}, \tag{41}$$

$$\sigma_{\phi z}^i = -i\mu\beta e^{i\beta z}\sin\phi e^{-i\omega t}, \tag{42}$$

$$\sigma_{r\phi}^i = \sigma_{rr}^i = \sigma_{zz}^i = \sigma_{\phi\phi}^i = 0, \tag{43}$$

It is obvious that the displacement and stress fields are asymmetric about the $\phi = 0$ axis.

For later use when satisfying the continuity conditions, an array containing the amplitudes of the nodal displacements on the boundary, $\{\bar{q}_B^i\}$, can be constructed by evaluating Eqs. (38)–(40) at each node on the boundary B. Similarly, an array containing the amplitudes of the nodal forces on the boundary, $\{\bar{P}_B^i\}$, can also be constructed from Eqs. (41)–(43). Each of these arrays will have $3N_B$ elements.

3.3. Global solution

The continuity of displacements and stresses across the boundary B can be imposed by setting the displacements and stresses from the interior region to be equal to those from the exterior region:

$$\{q_B\} = \{q_B^i\} + \{q_B^s\}, \tag{44}$$

$$\{P_B\} = \{P_B^i\} + \{P_B^s\}, \tag{45}$$

Since the ϕ-variation of the displacement and force components in both interior and exteriors regions are similar, Eqs. (44) and (45) can be written in terms of the amplitudes as

$$\{\bar{q}_B\} = \{\bar{q}_B^i\} + \{\bar{q}_B^s\}, \tag{46}$$

$$\{\bar{P}_B\} = \{\bar{P}_B^i\} + \{\bar{P}_B^s\}, \tag{47}$$

In view of Eqs. (46), (47) and (36), Eq. (14) takes the form

$$\begin{bmatrix} S_{II} & S_{IB} \\ S_{BI} & S_{BB} - S_f \end{bmatrix} \begin{Bmatrix} \bar{q}_I \\ \bar{q}_B \end{Bmatrix} = \begin{Bmatrix} 0 \\ \bar{P}_B^i - S_f \bar{q}_B^i \end{Bmatrix}. \tag{48}$$

Once the above equation is solved for the nodal displacements, the stress field in the interior region can be obtained from conventional procedures used in finite element analysis.

4. Numerical results and discussion

In this study, the dynamic excitation is provided by an incident SV-wave defined by Eq. (37). In the absence of the cavity, the stress field at any point in the medium can be expressed in rectangular coordinates as

$$\sigma_{xz} = \sigma_{zx} = i\beta\mu e^{i\beta z - i\omega t} \tag{49}$$

with all other stress components being zero. The maximum value of the stresses is $\mu\beta$.

In the presence of the cavity, the stress field is significantly different from that given by Eq. (49) due to scattering. The nonzero stresses on the surface of the cavity are σ_{tt}, $\sigma_{\phi\phi}$ and $\sigma_{t\phi}$ where **t** is the tangential vector on the surface of cavity as shown in Fig. 1a. The results have the general form

$$\sigma = (R + iI) f(\phi) e^{-i\omega t}, \tag{50}$$

where the $f(\phi)$ is either $\cos\phi$ or $\sin\phi$, the real part R represents the solution at $t = 0$ and $T/2$, and the imaginary part I represents the solution at $t = T/4$ and $3T/4$, T being the period of excitation. The absolute value $(R^2 + I^2)^{1/2}$ is the maximum stress which occurs at some instant of time depending on the phase-shift.

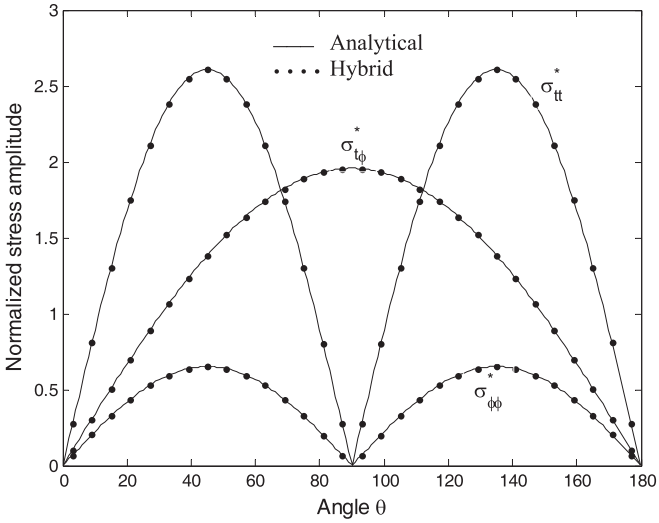

Fig. 3. Comparison of stresses along the circumference of a spherical cavity for $\omega^* = 0.01$.

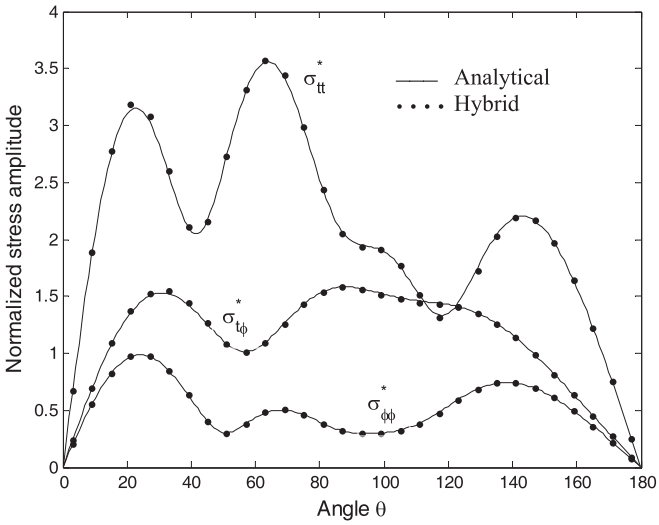

Fig. 4. Comparison of stresses along the circumference of a spherical cavity for $\omega^* = 3.0$.

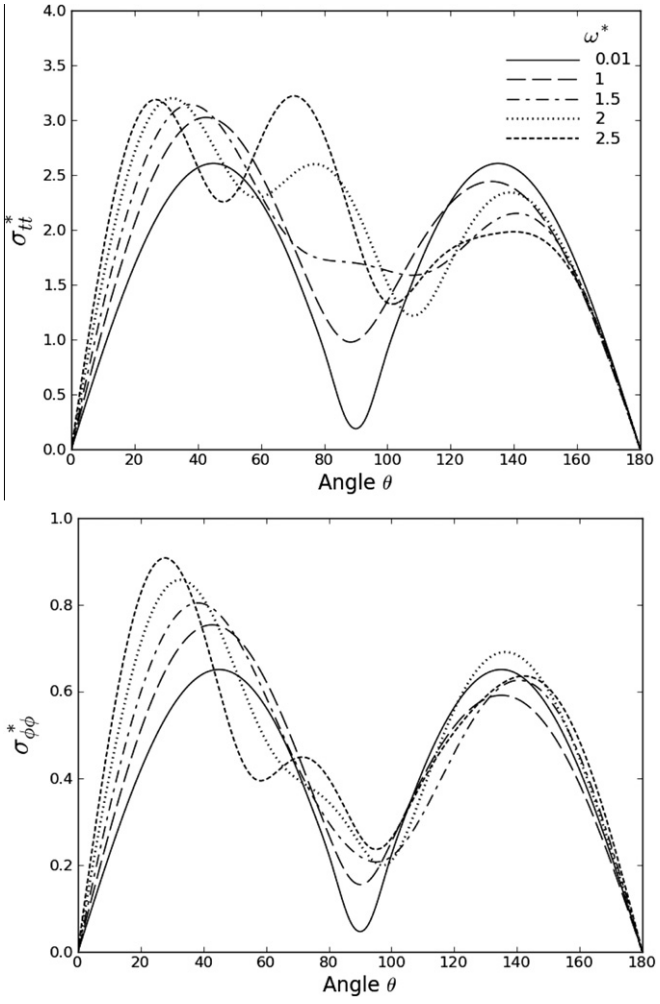

Fig. 5. Angular distribution of stresses on the surface of the cavity ($\nu = 0.25, b/a = 1$).

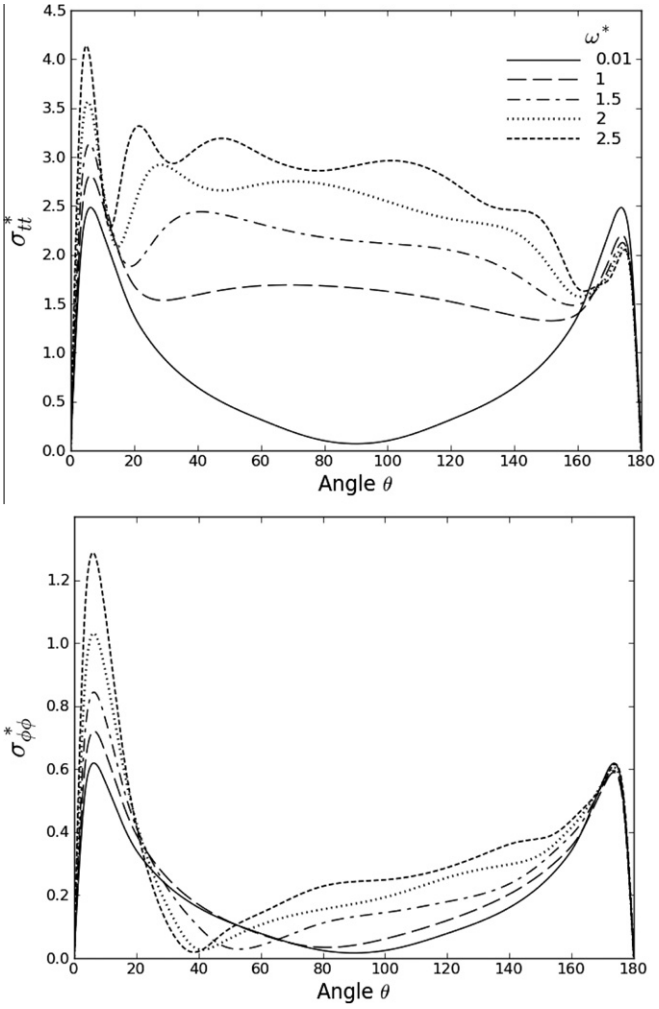

Fig. 6. Angular distribution of stresses on the surface of the cavity ($\nu = 0.25, b/a = 3$).

These stresses are expressed in dimensionless form by normalizing with respect to the maximum value of the incident stress field, $\mu\beta$:

$$\sigma^*_{ij} = \frac{|\sigma_{ij}|}{\mu\beta} \quad i,j = t,\phi. \tag{51}$$

Thus the values of σ^*_{ij} can be considered as dynamic stress concentration factors (Pao and Mow, 1973). They depend on the aspect ratio of the cavity and the frequency of excitation; the latter is expressed in nondimensional form through

$$\omega^* = \omega a\sqrt{\frac{\rho}{\mu}}, \tag{52}$$

where a, as defined earlier, is the radius of the cavity in the x–y plane.

The nature of the dynamic excitation is better appreciated by considering the limiting static case. When the frequency approaches zero, the applied stress field at infinity approaches

$$\sigma_{xz} = \sigma_{zx} = \sigma_0, \tag{53}$$

$$\sigma_{xx} = \sigma_{yy} = \sigma_{zz} = \sigma_{xy} = \sigma_{yz} = 0, \tag{54}$$

where σ_0 is a constant. The stress field of Eqs. (53 and 54) is pure shear. Thus, the results presented herein are for the dynamic counterpart of this shear load.

In order to assess the accuracy of the numerical procedure, stresses on the surface of a spherical cavity of radius a were computed by the present method and compared with the analytical solution. In Figs. 3 and 4, the results are presented in nondimensional form for two representative values of nondimensional frequencies of 0.01 and 3.0. Agreement between the analytical and numerical results can be seen to be excellent for both frequencies. The wave length corresponding to the nondimensional frequency of 0.01 is approximately 300 times the diameter of the cavity. Therefore the dynamic effects are not expected to be significant at this wave length and the dynamic solution must be close to the static solution corresponding to the loads given by Eqs. (53) and (54). A separate static analysis indeed confirmed that the two solutions hardly differed. In contrast, the dynamic solution for the nondimensional frequency of 3.0 is quite different from the solution corresponding to the nondimensional frequency of 0.01. This is because at the higher frequency, the wave length is about the same size as the diameter of the cavity and significant dynamic interaction is expected.

The accuracy of the hybrid model is influenced by three factors. First, the fineness of the mesh will obviously affect the results. It must be gradually increased until convergence is reached. Second, the number of wave functions p considered in Eqs. (32) and (33) will also affect the results. In theory, p must be less than or equal to N_B. In addition, p must be sufficiently large to guarantee convergence of the series in Eqs. (20)–(22), and (26)–(28). A simple strategy to satisfy these requirements is set p equal to N_B and gradually

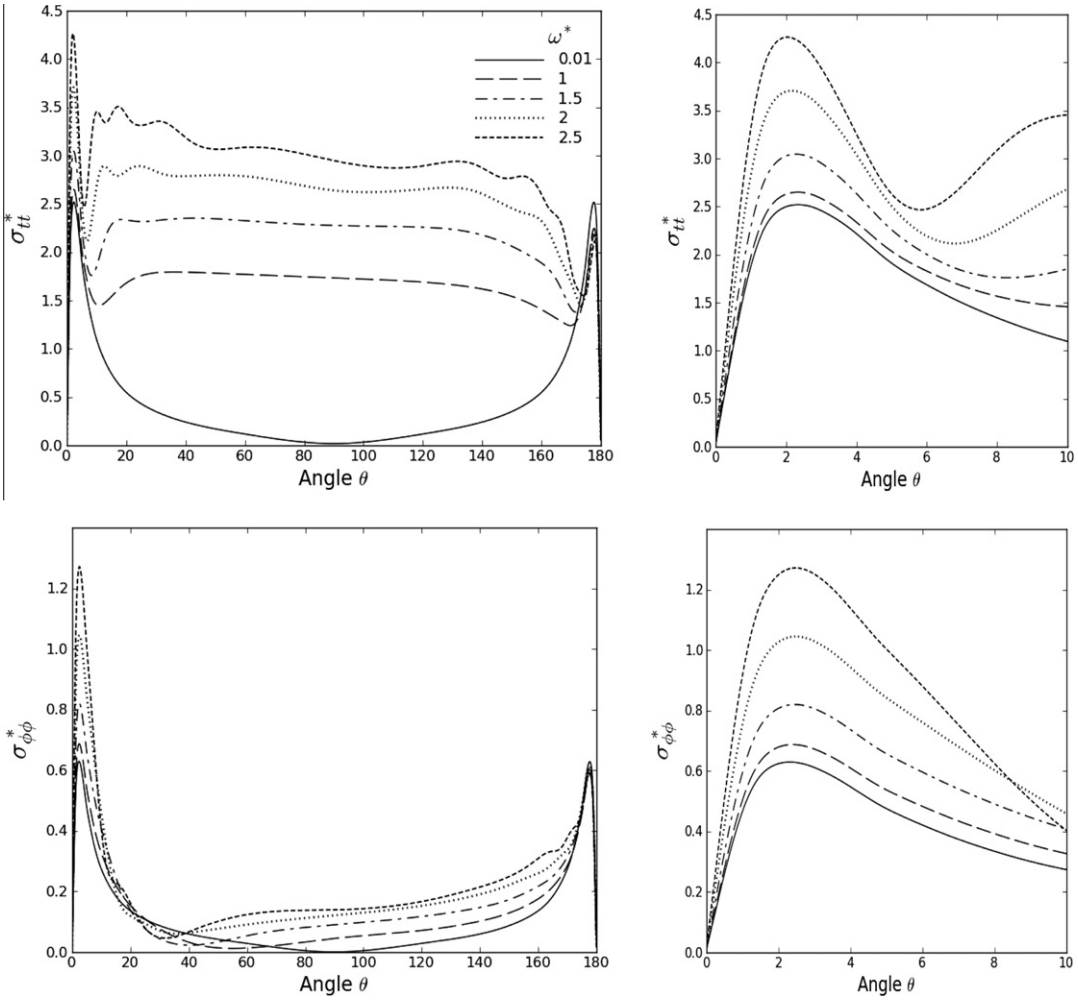

Fig. 7. Angular distribution of stresses on the surface of the cavity ($\nu = 0.25, b/a = 5$).

refine the mesh which, in turn, increases both N_B and p. While this worked well for low frequencies, numerical underflow and overflow problems were encountered at high frequencies. The numerical instability was caused by the magnitudes of Bessel and Hankel functions since, for p number of wave functions, the highest order of Bessel and Hankel functions to be evaluated is $p + 1$ and the magnitudes of these functions increases at a rapid rate with the order. Our recommendation is to start with $p = N_B/2$ and refine the mesh. This worked well for all frequencies. The last factor the influences the accuracy of the results is the location of boundary B. The radius of this boundary, R_B, should be large enough to completely enclose the cavity. However, a very large R_B is undesirable since the arguments of the Bessel and Hankel functions linearly increase with R_B and the algorithms available to calculate Bessel and Hankel functions become moderately less accurate for large arguments. It is therefore recommended that R_B be kept in the range of $1.1b$–$1.5b$, where b is the larger semi-axis of the cavity.

We shall now consider a spheroidal cavity. The problem can be solved analytically by using spheroidal coordinates. The mathematics of this approach is, however, complex and intricate. The problem is solved in this work by using the hybrid approach described earlier. Figs. 5–7 illustrate the angular distribution of σ^*_{tt} and $\sigma^*_{\phi\phi}$ for three cavity aspect ratios and five nondimensional frequencies. The stress component $\sigma^*_{t\phi}$ is not shown since its values consistently fall between those of σ^*_{tt} and $\sigma^*_{\phi\phi}$. It can be seen that both the nondimensional frequency and the cavity aspect ratio have a significant influence on the stress distribution. At the nondimensional frequency of 0.01, hardly any dynamic effect is expected and the dynamic solution can be regarded as a quasi-static one. The corresponding loading is given by Eqs. (53) and (54) which exhibit antisymmetry with respect to the $z = 0$ plane. The corresponding solution for stresses must exhibit antisymmetry with respect to the $z = 0$ plane. However, when the absolute values are plotted, they should exhibit symmetry. One can see in Figs. 5–7 that this is indeed the case for all aspect ratios. In addition, the maximum values of σ^*_{tt} and $\sigma^*_{\phi\phi}$ for $b/a = 1$ occur at 45° and 135°. As the cavity aspect ratio increases from unity the position of maximum stress moves progressively towards the poles. For reasons of clarity, stresses around a small region near the pole have been highlighted in Fig. 7. When the nondimensional frequency increases from 0.01, considerable scattering takes place and this changes the stress distribution. It can be seen that the maximum values of σ^*_{tt} are always greater than 1 in the range of frequencies considered. This indicates stress concentration. In addition, stress concentration values as high as 4.3 can be seen for σ^*_{tt} in Fig. 7. It is somewhat surprising to note that the stress peaks on the incident side of the cavity are lower than those on the shadow side. This effect is more prominent for higher frequencies.

The influence of frequency on the peak stress concentration values for σ^*_{tt} and $\sigma^*_{\phi\phi}$ is shown in Fig. 8 for various aspect ratios. Solutions for nondimensional frequencies higher than 2.5 for $b/a = 5$ could not be obtained due to numerical overflow problems. Various matrix conditioning schemes were tried with little success. For all aspect ratios, the peak stress concentration values are seen

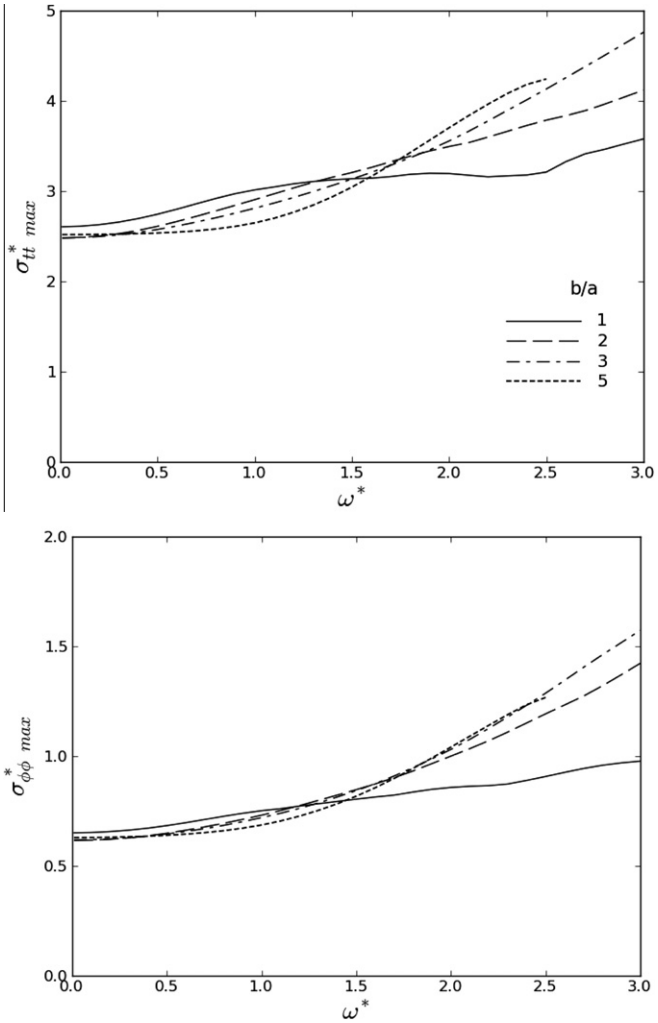

Fig. 8. Effect of cavity aspect ratio b/a on peak stress concentration values ($\nu = 0.25$).

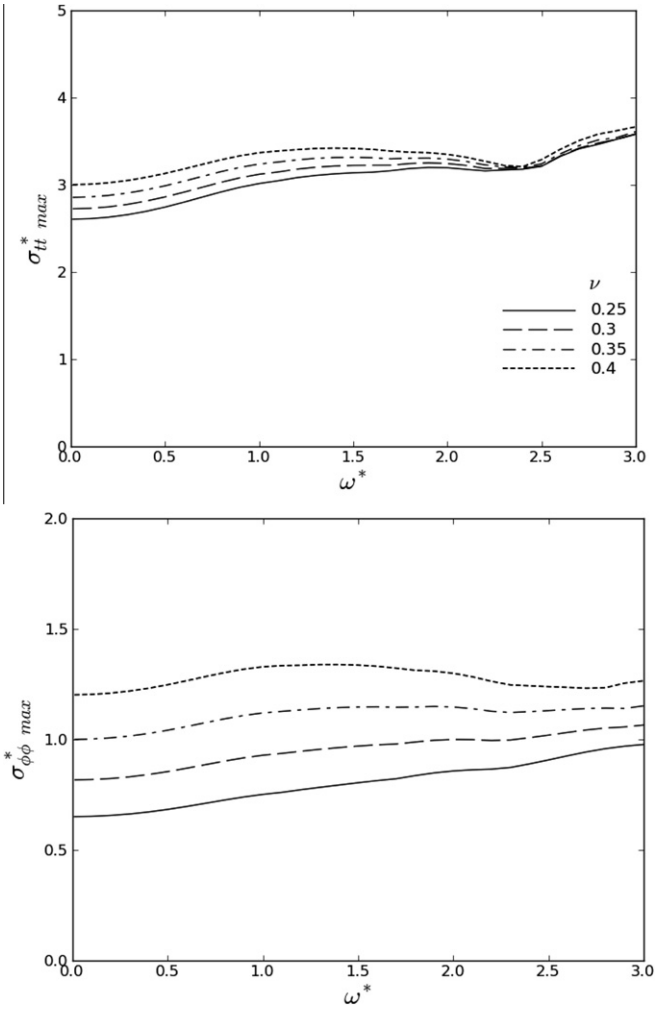

Fig. 9. Effect of Poisson's ratio on stress concentration values ($b/a = 1$).

to increase with frequency. For nondimensional frequencies higher than 1.7, increase in aspect ratio corresponds with an increase in the peak stress value for any given frequency. However, this trend is reversed for nondimensional frequencies lower than 1.5. While the maximum static stress concentration is around 2.5, the maximum calculated dynamic stress concentration of 4.76 occurs for $b/a = 3$ at $\omega^* = 3.0$. This corresponds to a 90% increase in dynamic stress concentration from the static value.

Figs. 9 and 10 depict the effect of the material Poisson's ratio. An increase in the Poisson's ratio of the medium is seen to increase the dynamic stress concentration and this effect is more pronounced for $\sigma^*_{\phi\phi}$ than for σ^*_{tt}. Despite this, σ^*_{tt} still dominates since its values are much higher than those of $\sigma^*_{\phi\phi}$.

5. Concluding remarks

A hybrid method has been presented to study the stress concentration around a cavity embedded in an elastic medium. The method combines the finite element technique with spherical wave functions to obtain the solution. The accuracy of the method was verified by analyzing a spherical cavity. The results from the hybrid method compare well with those obtained analytically. The results for a spheroidal cavity indicate that the dynamic stress concentration is strongly influenced by the excitation frequency, the aspect ratio of the cavity and the Poisson's ratio of the material. In general, the dynamic stress concentration factors are considerably higher than the quasi-static values, and in certain cases, they can be as high as 90% more than the quasi-static value.

Acknowledgements

The work reported herein was supported in part by a grant from the Centre of Excellence in Strong Materials, University of the Witwatersrand. Support was also received from the National Research Foundation.

Appendix A

Assuming $\{\bar{q}^s_B\}_{sph}$ is known, Eq. (32) may be solved for $\{a\}$ by minimizing the least square error of the error function $\{\epsilon\}$ defined by

$$\{\epsilon\} = [G]\{a\} - \{\bar{q}^s_B\}_{sph}. \tag{A1}$$

The square of the error ϵ^2, which is a scalar, is given by

$$\epsilon^2 = \{\epsilon^*\}^T\{\epsilon\}. \tag{A2}$$

Substitution of (A1) in (A2) leads to

$$\epsilon^2 = \{a^*\}^T[G^*]^T[G]\{a\} - \{\bar{q}^{s^*}_B\}^T_{sph}[G]\{a\} - \{a^*\}^T[G^*]^T\{\bar{q}^s_B\}_{sph} + \{\bar{q}^{s^*}_B\}^T_{sph}\{\bar{q}^s_B\}_{sph}. \tag{A3}$$

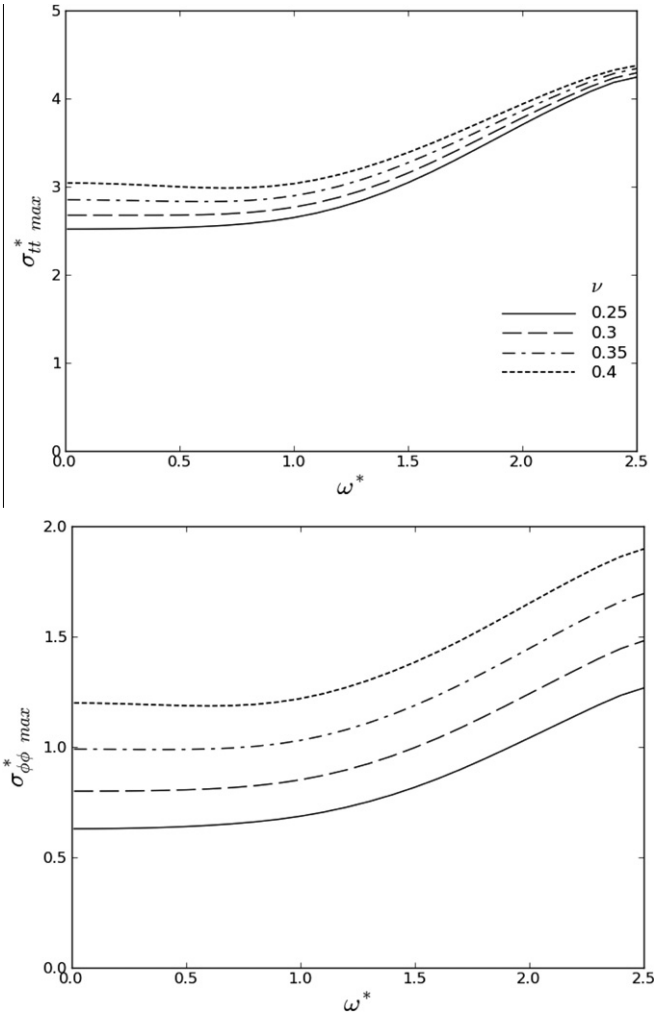

Fig. 10. Effect of Poisson's ratio on stress concentration values ($b/a = 5$).

Minimizing the square of the error with respect to $\{a\}$ yields

$$[G^*]^T[G]\{a\} = [G^*]^T\{\bar{q}^s_B\}_{sph}. \tag{A4}$$

Since $[G^*]^T[G]$ is a square matrix, the equation (A4) can be solved for $\{a\}$ as

$$\{a\} = [H]\{\bar{q}^s_B\}_{sph}, \tag{A5}$$

where

$$[H] = \left([G^*]^T[G]\right)^{-1}[G^*]^T. \tag{A6}$$

For $p \leqslant N_B$, $[H]$ is the generalized inverse of $[G]$ and the uniqueness of the operation is assured (Lancaster, 1969).

References

Boccaccini, A.R., 1998. Influence of stress concentrations on the mechanical property-porosity correlation in porous materials. J. Mater. Sci. Lett. 17, 1273–1275.

Boccaccini, A.R., Ondracek, G., Mombello, E., 1995. Determination of stress concentration factors in porous materials. J. Mat. Sci. Lett. 14, 534–536.

Bogan, S.D., Hinders, M.K., 1993. Dynamic stress concentration in fibre-reinforced composites with interface layers. J. Compos. Mat. 27, 1272–1311.

Cook, R.D., Malkus, D.S., Plesha, M.E., 1989. Concepts and applications of finite element analysis, third ed. John Wiley & Sons, New York.

Danninger, H., Jangg, G., Weiss, B., Stickler, R., 1993. Microstructure and mechanical properties of sintered iron. Part 1: basic considerations and review of literature. Powder Metall. Int. 25, 111–117.

Datta, S.K., 1977. Diffraction of plane elastic waves by ellipsoidal inclusions. J. Acoust. Soc. Am. 61, 1432–1437.

Eshraghi, H., Dravinski, M., 1989a. Scattering of plane harmonic SH, SV, P and Rayleigh waves by non-axisymmetric three-dimensional canyons: a wave function expansion approach. Earthq. Eng. Struct. Dyn. 18, 983–998.

Eshraghi, H., Dravinski, M., 1989b. Scattering of elastic waves by nonaxisymmetric three-dimensional dipping layer. Numer. Methods Partial Differ. Equat. 5, 327–345.

Fang, X.Q., Liu, J.X., Wang, X.H., Zhang, T., Zhang, S., 2009. Dynamic stress from a cylindrical inclusion buried in a functionally graded piezoelectric material layer under electro-elastic waves. Compos. Sci. Tech. 69, 1115–1123.

Givoli, D., 1991. Non-reflecting boundary conditions. J. Comput. Phys. 94, 1–29.

Hasselman, D.P.H., Fulrath, R.M., 1964. Effect of small fraction of spherical porosity on elastic moduli of glass. J. Am. Ceram. Soc. 47, 52–53.

Hayir, A., Bakirtas, I., 2004. A note on plate having a circular cavity excited by plane harmonic SH waves. J. Sound Vib. 27, 241–255.

Iturrarán-Viveros, U., Sánchez-Sesma, F.J., Luzón, F., 2008. Boundary element simulation of scattering of elastic waves by 3-D cracks. J. Appl. Geophys. 64, 70–82.

Kirsch, G., 1898. Die Theorie der Elastizität und die Bedurfnisse der Festigkeitslehre. Z. Ver. Dtsch. Ing. 42, 797.

Lancaster, P., 1969. Theory of Matrices. Academic Press, New York.

Lee, V.W., 1984. Three dimensional diffraction of plane P, SV, and SH waves by a semispherical alluvial valley. J. Soil Dyn. Earthq. Eng. 3, 133–144.

Maitra, A.K., Phani, K.K., 1994. Ultrasonic evaluation of elastic parameters of sintered compacts. J. Mater. Sci. 29, 4415–4419.

Manolis, G.D., Beskos, D.E., 1988. Boundary Element Methods in Elastodynamics. Allen & Unwin Inc., Winchester, Mass. 01890, USA.

Meguid, S.A., Wang, X.D., 1997. Wave scattering from partially-debonded inhomogeneities in advanced ceramics. Presented at The 1997 Joint ASME, ASCE and SES Summer Metting, June 29–July 2, Northwestern University.

Mossessian, T.K., Dravinski, M., 1989c. Scattering of elastic waves by three dimensional surface topographies. Wave Motion 11, 579–592.

Mossessian, T.K., Dravinski, M., 1990. Amplification of elastic waves by a three dimensional valley. Part 1: steady state response. Earthq. Eng. Struct. Dyn. 19, 667–680.

Neuber, H., Hahn, H.G., 1966. Stress concentration in scientific research and engineering. Appl. Mech. Rev. 19, 187–199.

Panakkal, J.P., Willems, H., Arnold, W., 1990. Nondestructive evaluation of elastic parameters of sintered iron powder compacts. J. Mater. Sci. 25, 1397–1402.

Pao, Y.H., Mow, C.C., 1973. Diffraction of Elastic Waves and Dynamic Stress Concentration. Crane and Russak, New York.

Paskaramoorthy, R., Meguid, S.A., 1999. Large internal stresses in particulate-reinforced composites subjected to dynamic loads. Compos. Sci. Tech. 59, 1361–1367.

Paskaramoorthy, R., Meguid, S.A., 2000. On the dynamic behaviour of porous materials. Int J. Solid Struc. 37, 2341–2358.

Paskaramoorthy, R., Datta, S.K., Shah, A.H., 1988. Effect of interface layers on scattering of elastic waves. J. Appl. Mech. 55, 871–878.

Paskaramoorthy, R., Bugarin, S., Reid, R.G., 2009. Effect of an interphase layer on the dynamic stress concentration in a Mg-matrix surround SiC particle. Compos. Struct. 91, 451–460.

Prokic, A., Lukic, D., Anagnosti, P., 2009. Stress–strain field around elliptic cavities in elastic continuum. Eur. J. Mech. 28, 86–93.

Sanchez-Sesma, F.J., 1983. Diffraction of elastic waves by three dimensional surface irregularities. Bull. Seism. Soc. Am. 73, 1621–1636.

Sarma, G.S., Mallick, K., Gadhinglajkar, V.R., 1998. Nonreflecting boundary condition in finite-element formulation for an elastic wave equation. Geophys. 63, 1006–1016.

Sternberg, E., 1958. Three-dimensional stress concentrations in the theory of elasticity. Appl. Mech. Rev. 11, 1–4.

Tan, S.C., 1994. Stress Concentrations Laminated Composites. Technomic Publishing Co, Lancaster, PA, USA.

Wang, J.C., 1984. Young's modulus of porous materials. J. Mater. Sci. 19, 801–814.

Wang, J.H., Zhou, X.L., Lu, J.F., 2005. Dynamic stress concentration around elliptic cavities in a saturated poreelastic soil under harmonic plane waves. Int. J. Solids Struct. 42, 4295–4310.

Willis, J.R., 1980. A polarization approach to the scattering of elastic waves – I. Scattering by a single inclusion. J. Mech. Phys. Solids 28, 287–305.

Yang, Z., Kima, C.B., Choa, C., Beoma, H.Y., 2008. The concentration of stress and strain in finite thickness elastic plate containing a circular hole. Int. J. Solids. Struct. 45, 713–731.

Ying, C.F., Truell, R., 1956. Scattering of a plane longitudinal wave by a spherical obstacle in an isotropically elastic solid. J. App. Phys. 27, 1086–1097.

Yu, C.W., Dravinski, M., 2009. Scattering of a plane harmonic SH wave by a completely embedded corrugated scatterer. Int. J. Numer. Methods Eng. 78, 196–214.

Yu, P., Guo, W., Shea, C., Zhaoa, J., 2008. The influence of Poissons ratio on thickness-dependent stress concentration at elliptic holes in elastic plates. Int. J. Fatigue 30, 165–171.